ACS APPLIED MATERIALS & INTERFACES

Article

SERS active nano-biosensor functionalized by self-assembled 3D nickel nanonetworks for glutathione detection

Sivaprasad Chinnakkannu Vijayakumar, Krishnan Venkatakrishnan, and Bo Tan

ACS Appl. Mater. Interfaces, **Just Accepted Manuscript** • Publication Date (Web): 24 Jan 2017

Just Accepted

ACS Publications

ACS Applied Materials & Interfaces is published by the American Chemical Society.
1155 Sixteenth Street N.W., Washington, DC 20036

SERS active nano-biosensor functionalized by self-assembled 3D nickel nanonetworks for glutathione detection

Authors: Sivaprasad Chinnakkannu Vijayakumar[1]; Krishnan Venkatakrishnan[1, 1*‡]; Bo Tan[2]

[1]Micro/Nanofabrication facility, Department of Mechanical and Industrial Engineering, Ryerson University, 350 Victoria street, Toronto, Ontario, M5B 2K3, Canada

[1*]Affiliate Scientist, Keenan Research Center, St. Michael's Hospital, 209 Victoria Street, Toronto, Ontario M5B 1T8, Canada

[2]Nanocharacterization Laboratory, Department of Aerospace Engineering, Ryerson University, 350 Victoria Street, Toronto, Ontario, M5B 2K3, Canada

[‡] Corresponding Author: venkat@ryerson.ca 416-979-5000 Ext: 4984

Abstract:

We introduce a "non-noble metal" based SERS active nano-biosensor using a self-assembled 3D hybrid nickel nanonetwork. A tunable biomolecule detector fabricated by a bottom-up approach was functionalized using a multiphoton ionization energy mechanism to create a self-assembled 3D hybrid nickel nanonetwork. The nanonetwork was tested for SERS detection of crystal violet (CV) and glutathione (GSH) at two excitation wavelengths, 532 nm and 785 nm. The results reveal indiscernible peaks with a limit of detection (LOD) of 1 picomolar (pM) concentration. An enhancement factor (EF) of 9.3×10^8 was achieved for the chemical molecule CV and 1.8×10^9 for the biomolecule GSH, which are the highest reported values so far. The two results, one being the CV molecule proved that nickel nanonetwork is indeed SERS active and the second being the GSH biomolecule detection at both 532 nm and 785 nm, confirm that the nanonetwork is a biosensor which has potential for both in-vivo and in-vitro sensing. In addition, the selectivity and versatility of this biosensor is examined with biomolecules such as L-Cysteine, L-Methionine and sensing GSH in cell culture medium which mimics the complex biological environment. The functionalized self-assembled 3D hybrid nickel nanonetwork exhibits electromagnetic and charge transfer based SERS activation mechanisms.

Keywords: Self-assembled; 3D nickel nanonetwork; SERS activation; nano biosensor; Glutathione; Crystal Violet; L-Cysteine; L-Methionine;

1. Introduction:

The development of functionalized nanomaterials has attracted considerable interest in the field of diagnostics and bio sensing because nanometer-scale materials offer several properties that bulk

materials lack[1,2]. A significant challenge in bioanalytical sensing is the development of highly sensitive platforms that overcome the limitations of conventional sensing techniques, which include electrochemical[3–5], piezo-electric[6], and thermometric sensing[7]. With the increasing usage of gold nanoparticles, optical sensing techniques, such as UV-Vis spectroscopy, resonance elastic light scattering, fiber optics sensing, and spectrofluorometric sensing, have gained much attention in biomedical science because of their increased sensitivity, improved spatial resolution, and throughput capability[8–10]. Among the various optical sensing mechanisms, surface enhanced Raman scattering (SERS) is most valuable owing to its non-invasive nature, higher sensitivity, and broad range of excitation wavelengths with various nanomaterials. SERS enhancement offers unique spectral molecular fingerprint data from the interaction area with limited photo bleaching, reduced background interference, auto fluorescence, and high sensitivity, as compared with other optical detection techniques such as fluorescence and electrochemical sensing[11]. Numerous semiconductor-based nanomaterials, such as TiO_2, ZnO, graphene, and CuTe, have been reported to be SERS platforms, but their enhancements (~10^2–10^4) are relatively weak compared to enhancements provided by SERS platforms based on noble transition metals (~10^4–10^8)[3,12,13]. Noble-metal monolayer-coated semiconductor hybrid nanostructures with varying morphologies have also been used as SERS substrates for multi-analyte detection[14–16]. Noble-metal-based nanomaterials have demonstrated superior properties in terms of increased SERS sensitivity by the tuning of their optical absorption properties, band gap, and excitation Bohr radius[17,18]. This has enabled detection at very low concentrations of analytes and has even led to the possibility of single molecule detection with SERS enhancement factors ranging from ~10^6 to 10^{12} by using noble-metal-based nanomaterials[19–21]. Therefore, most current research is devoted to developing either noble metals or noble-metal-coated semiconductor nanomaterials as SERS active substrates.

Noble metals exhibit localized surface plasmon resonance (LSPR) when excited by photons. Apart from SPR, charge transfer resonance and hotspots are also hypothesized to contribute towards SERS enhancement in both semiconductor and metal-based nanostructures[17,18]. Investigations have also revealed that nanostructure morphology plays a pivotal role in inducing SERS exertion. Noble metal nanostructures, including nanostars, nanofilms, nanocarpets, nanorods and hollow or solid nanocubes, have been synthesized for investigation in this direction[22–25]. However, noble metal and semiconductor–noble-metal hybrid nanomaterials have several limitations making them undesirable for a variety of biomedical applications. Noble-metal-based substrates are often synthesized using chemical reduction, oxidation, or physical deposition processes, which lead to poor biocompatibility and thereby severely

limit their use as biomolecular sensing materials[26]. As a result, the need for "non-noble metal" based SERS active nanostructured material with strong biocompatibility is of utmost importance for bio-sensing applications. In this regard, nickel nanomaterials have received considerable attention. Being a prime magnetic transition material with excellent biocompatibility, nanoscale nickel is extensively used as contrast agents for MRI diagnosis, hyperthermia, and cancer therapeutic applications[27,28]. However, results reveal that nickel nanowires synthesized by electrochemical process are Raman insensitive because of the inherent characteristics of nickel. Interestingly, gold coated nickel nanowires fabricated by the same method are noted to be Raman active[29].

Some studies have prepared nickel-based nanostructures for SERS with conventional fabrication techniques, including galvanic displacement, redox transmetalation, and electrochemical synthesis. Sanjanlal et al. used the galvanic displacement technique to fabricate nickel nanowires and nanocarpets coated with noble metals (Au, Ag) for facilitating SERS sensing of trace analytes[30]. Similarly, Manoj et al. demonstrated the Raman detection of methylene blue analyte by using composite Ni/Ag nano flowers fabricated by redox transmetalation[31]. By adopting an electrochemical technique, Bayata et al. reported the fabrication of a honeycomb template with nickel nanowires self-assembled inside anodic aluminum oxide. A thin layer of gold was deposited on the honeycomb. In these experiments, the SERS was found to be enhanced by the gold nanoparticles. The nickel nanostructures acted as a carrier of the gold nanoparticle and a platform to attract and adhere biomolecules, and they in no way assisted in actively inducing Raman scattering. Thus, these highly anisotropic nanomaterials fabricated using solution-based methods are dependent on the use of noble metal coatings such gold and silver to accomplish SERS enhancement at 532 and 785 nm[29]. Hence, there is a significant incentive to fill the need of SERS active nickel-based nanostructures, which will further the development of optical-based detection nano-biosensor platforms and reduce the reliance on noble metals as SERS activators.

In this research, we developed a nano-biosensor using a functionalized hybrid nickel nanonetwork for biomolecule sensing and detection. The self-assembled 3D hybrid nickel nanonetwork is functionalized by multiphoton ionization induced by a high-energy femtosecond laser. The nanonetwork can activate Raman detection of crystal violet (CV) and glutathione (GSH) molecules at 1 pM (~1×10^{-12}M) concentrations at two excitation wavelengths, 532 nm and 785 nm. An enhancement factor of 10^9, a level not observed before even with noble metal monolayer coatings, is seen here. This extends the limit of detection (LOD), making the self-assembled 3D hybrid nickel nanonetwork a promising "non-noble metal" based candidate for chemical and biomolecular sensing. The 3D hybrid nickel nanonetwork proposed here could open up new vistas in the field of nano-biosensors.

2. Materials and Methods:

2.1 Materials:

Commercially available Nickel 200 sheets (3 mm thickness) having 99% nickel were used in all experiments. The surface was subjected to gradual mechanical polishing using SiC grit sandpaper (240–600) and later ultra-sonically cleaned in 100% acetone and ethanol for a duration of 15 min each to remove all embedded particle inclusions during polishing.

2.2 Preparation of Crystal Violet Substrate:

Crystal violet dye was selected because of its large Raman cross-section, and it is used often for testing Raman scattering. A stock solution of CV was prepared from anhydrous powder purchased from Sigma Aldrich to an initial concentration of 1 M and sequentially diluted to 1×10^{-3} M, 1×10^{-6} M, 1×10^{-9} M, and 1×10^{-12} M with ultra-pure water for experimentation.

2.3 Preparation of Glutathione Substrate:

L-Glutathione reduced powder was purchased from Alfa Aesar, and a stock solution was prepared using ultrapure water to 1 M concentration. A series of dilutions were made later using ultra-pure water to 1×10^{-3} M, 1×10^{-6} M, 1×10^{-9} M, and 1×10^{-12} M concentrations and kept in a refrigerator maintained at 4°C covered with metal foil to protect it from direct light.

2.4 Preparation of L- Cysteine Substrate:

L-Cysteine hydrochloride powder was purchased from Sigma Aldrich and a series dilution of 1mM and 1µM concentration was prepared with ultrapure water for experimentation.

2.5 Preparation of L-Methionine Substrate:

L-Methionine powder was purchased from Alfa Aesar and a series dilution of 1mM and 1µM concentration was prepared with ultrapure water for experimentation.

2.6 Preparation of complex biological substrate:

Biological cell culture medium DMEM-F12 medium was purchased from Gibco Life technologies.

2.7 Preparation of GSH with complex biological substrate:

The prepared L-Glutathione stock solution is diluted to $1x10^{-6}$M concentration using ultrapure water and further diluted to prepare 1µM concentration of GSH solution. A 10µL of this solution is then added to 1ml biological cell culture DMEM-F12 medium to prepare a complex biological GSH solution.

2.8 Multiphoton Ionization Procedure:

A diode-pumped Yb-doped fiber laser from Impulse series (Clark - MXR) having a central wavelength of 1030 nm and an average power of 16 W was employed for fabricating the self-assembled 3D hybrid nickel nanonetwork. To do this, an ultra-short pulsed laser (UPL) system having a varying laser pulse interaction time of 214 fs to 1428 fs with a laser pulse repetition rate between 4 and 25 MHz was made

to interact with the prepared nickel samples. The samples were mounted on x-y-z precision stages to steer the incoming laser beam. To maximize the effectiveness of the fabrication, some of the processing parameters were kept constant. The laser pulse interaction time was fixed at 214 fs, average power at 16 watts, and dwell time at 5 ms, which is the time spent delivering laser the pulses to a single point on the specified sample. Based on earlier studies using Clark-MXR Impulse series laser, a laser spot size of 1.02 µm was used for the creation on the 3D nanostructure. An array of ablation points was created on the target sample to obtain a workable quantity of 3D nanostructures. EzCAD software and a galvoscanner were deployed for the plotting. The experimental setup and fabrication procedure are presented in the inset of Figure 1. The ionization energy was varied in order to obtain the self-assembled 3D nanonetwork. The experimental parameters employed are listed in Table S1 along with their labels: Cuboidal, Spheroidal-Cuboidal, and Spheroidal nanonetworks.

2.9 Scanning Electron Microscope:

The fabricated nickel specimens were evaluated initially using an environmental scanning electron microscope (ESEM; Quanta FEG 250). To evaluate and study the effects induced by the multiphoton ionization energy on the fabricated 3D nanonetwork, a high resolution scanning electron microscope (HRSEM; Hitachi S5200) was employed. A carbon copper grid was used to collect the nanonetwork, and demangetized using a Neodymium magnet before examination. Then, an HRSEM\EDX attachment from Oxford Instruments was used to primarily analyze the elemental composition of the synthesized nanonetwork.

2.10 AFM Analysis:

To examine the oxide phases and morphological variations in the synthesized self-assembled 3D nanonetwork, an atomic force microscope (AFM; ND-MDT, Russia) was used. A prefabricated gold-coated silicon cantilever tip with a spring constant of 15 N/m is employed in both the contact and non-contact mode at a scan rate of 0.05 Hz each to acquire images at a scan area of 100 × 100 µm.

2.11 X-Ray Diffraction:

To quantitatively and qualitatively identify the oxide phase concentration, an X-ray diffraction (Phillips powder XRD) was employed with Cu K-α radiation (λ = 1.54054Å) at 40 KV and 40 mA with a 2ϑ scanning speed of 0.025° min^{-1} scanning a range from 30°–80°. Rietveldt analysis was carried on the acquired spectra, and crystallite size measurements of the nickel and nickel oxide nanoparticles formed within the 3D nanonetwork were estimated using the Scherrer equation.

2.12 Raman Spectroscopy:

The synthesized specimens were analyzed using a Bruker Senterra Dispersive Raman Microscope fitted with a multi-wavelength laser system (532 nm and 785 nm). An appropriate laser irradiation power of 5

and 10 mW is used with a standard collection time of 10 s with three repetitions. These parameters were chosen based on a previous trial and error method to reduce spectrum noise. A 50x objective was used to tightly focus the laser on the sample surface. All spectra are baseline corrected and normalized to laser power. The supporting information section describes the procedure that was used to determine the analytical enhancement factor (EF) value of the nickel nanonetwork.

2.13 Statistics:

All experiments were carried out thrice, and the data points were averaged, unless otherwise mentioned. The error bars represent standard deviation.

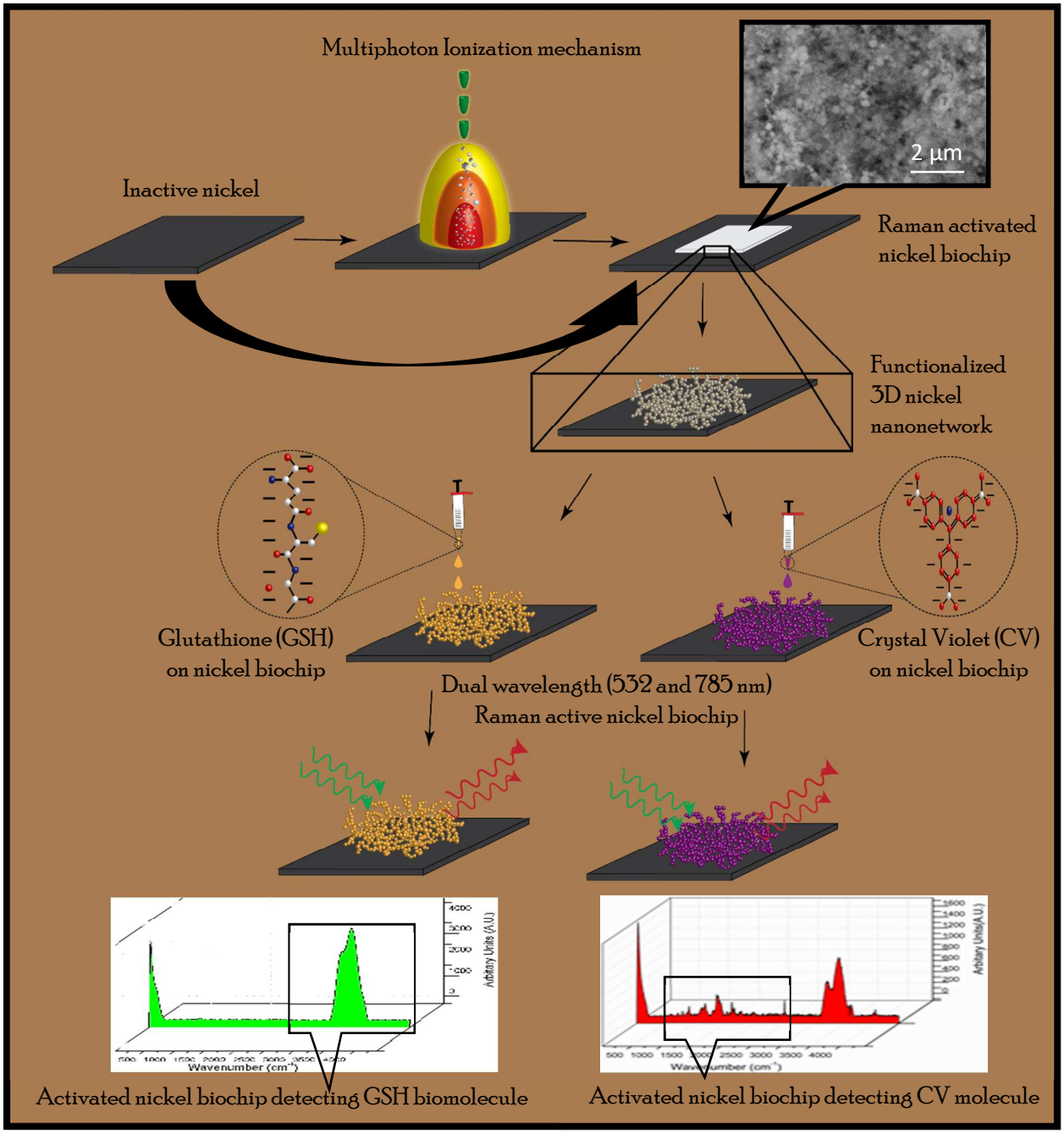

Figure 1: Functionalized 3D hybrid nickel nanonetwork fabrication on nickel biochip with dual wavelength Raman activation for GSH and CV detection

3. Results and Discussion:

3.1 Synthesizing Interdenominational Self-assembled 3D Hybrid Nickel Nanonetwork:

The formation of self-assembled 3D nanostructures synthesized using ionic condensation has been previously investigated[32]. When a laser beam shines on a solid target, the material absorbs the photon energy. The absorption depth for metals is usually several tens of nanometers, which is a very small

volume. Femtosecond lasers with extremely short pulse durations exhibit peak power as high as gigawatts. The small volume of material under irradiation absorbs the energy in a very short time, and thus undergoes a swift transformation from an initial cold solidified state to a high energy plasma state, where time-dependent ionization and material recombination occurs[12]. At the interface of the plasma and ambient atmosphere, more complicated chemical reactions occur between the ionized species and surrounding atmosphere molecules. This involves the formation of oxides and compounds having specific material properties (morphology, size, and oxide phase). Here, it is expected that the synthesized species, in the form of ions, atoms, or clusters, would strongly react with oxygen molecules in air to form Ni/NiO droplets, which are quenched rapidly. Because of the high kinetic energy of the expanding plasma, larger cooler droplets will be ejected out of the plasma, forming a self-assembled 3D hybrid nickel nanonetwork. By varying the laser parameters, the temperature of the plasma can be varied, which in turn alters the size, morphology, and composition of the formed 3D nanonetwork. Therefore, the properties of the 3D nanonetwork can be tuned to a certain extent.

3.2 Structure, morphology, and physical property analysis of the synthesized nanonetwork:

The controllability of the synthesized 3D self-assembled hybrid nickel nanonetwork on the nickel surface is demonstrated in the inset of Figure 2. Two types of particle shapes were observed, spherical particles and cubic particles, as shown in the inset of Figure 2. Nanonetworks generated by an ultra-short pulsed laser (UPL) are known to vary in size depending on the experimental conditions[33]. In addition, it was observed here that cuboidal particles were smaller in size, while most of the larger particles exhibited a spherical shape. The average particle sizes consistently decreased with increasing dwell time (number of incident laser pulses).

AFM contrast studies were carried out to analyze the height and phase composition of the synthesized 3D hybrid nickel nanonetwork. In comparison to the SEM images shown in the inset of Figure 2, the AFM images remain relatively uniform regardless of the 3D nanonetwork. It is worth noting that the sharp-edged nickel nanonetwork imaged in the insert of Figure 2 appears to be smooth in the AFM scan. Although, the AFM scan revealed areas of varying density of nanofibrous structures, the scan did not reveal the surface morphology of the 3D nickel nanonetwork. Thus, it is increasingly difficult to image the 3D flexible nanonetwork by using AFM and absorption/excitation of SERS. This uncertainty gets compounded with complex geometries observed in cuboidal and spheroidal-cuboidal nanonetwork SEM images, as shown by the cubic-shaped nanoparticles in the inset of Figure 2.

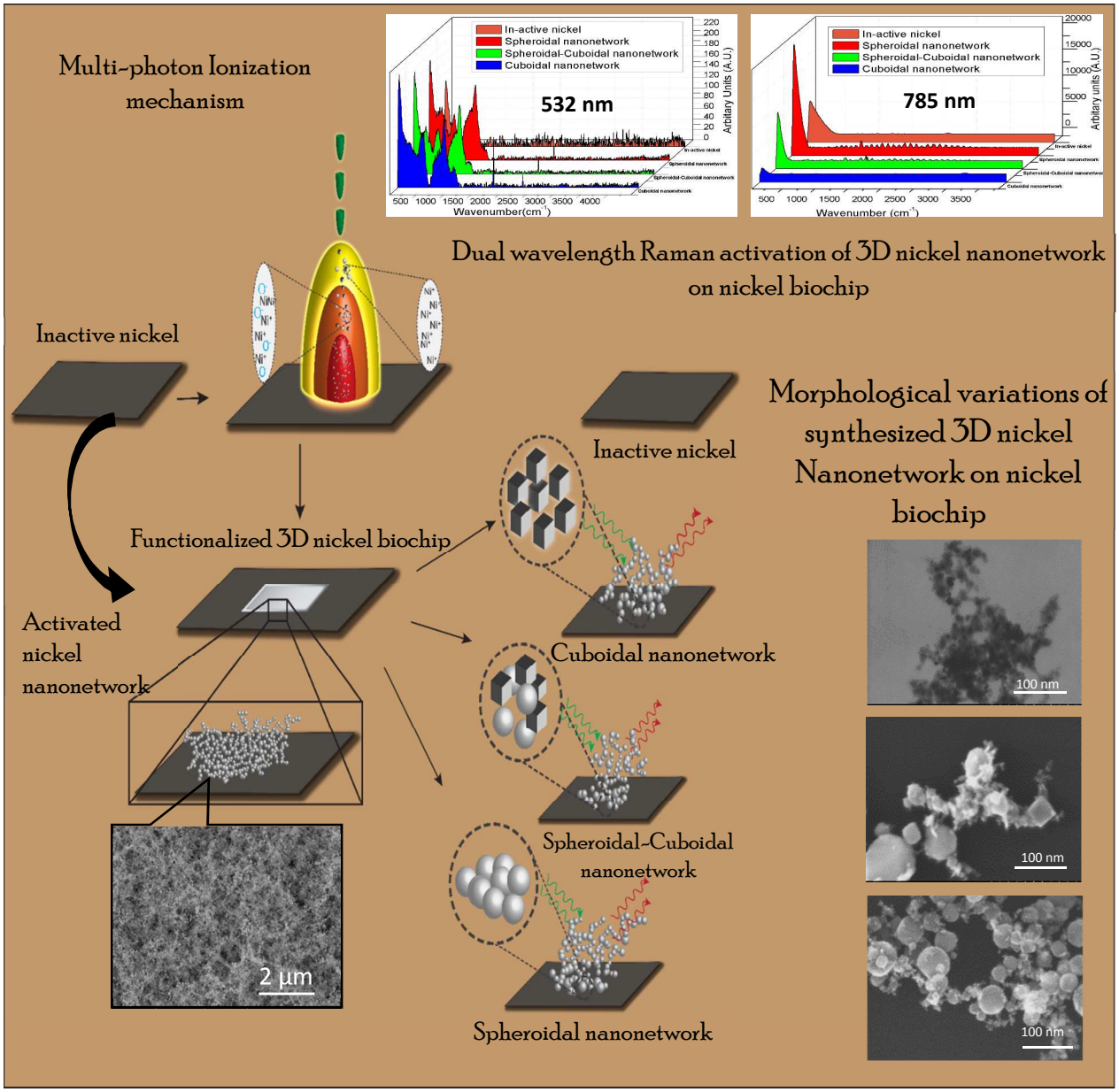

Figure 2: Synthesis of 3D nickel nanonetwork on nickel substrate using multi-photon ionization mechanism and subsequent Raman self-activation. The multiphoton ionization created cuboidal, spheroidal-cuboidal and spheroidal morphology nanonetwork

Constructive interference between the incident and reflected light can enhance the electro-magnetic effect with no apparent change in the plasmon resonance[34]. The plasmon width and red shifting are sensitive to the size and morphology of the suspended nanonetwork[35]. Therefore, the flexibility of the 3D nanonetwork with the suspended nanoparticles is affected by the network depth and porosity. The AFM height scans in the inset of Figure S1(A) shows that the cuboidal nanonetwork is denser than the spheroidal nanonetwork. The topographic image revealed that the interacting forces between the AFM tip and nanonetwork are not magnetic and involve the combined effect of electrostatic and Van der

Waals interactions. The XRD spectrum from the inset of Figure S1(C) shows a significant line broadening, which is a characteristic phenomenon of nickel/nickel oxide nanoparticles. The spectrum clearly shows that the nanonetwork is of a crystalline nature. The crystallite size was estimated from the XRD pattern using by Scherrer's equation, where the shape factor K = 0.9, X-ray wavelength of Copper (Cu) Kα = 1.54 Å, Bragg diffraction angle is θ, and β is the FWHM of the respective diffraction peak. The average crystallite size of the synthesized self-assembled 3D hybrid nickel nanonetwork was found to be approximately 50 nm, which is much larger than that observed from the TEM images in the inset of Figure 2.

The energy dispersive X-ray (EDX) analysis using FESEM on individual nanoparticles detected only elemental nickel and oxygen exclusive of substrate signals. The ratio of Ni and O is almost 1:1, supporting the formation of NiO. Further analysis did show that the composition remained consistent irrespective of particle size and shape. The line EDX images in the scanning–transmission (STEM) mode for the selected nanonetwork are showcased in the inset of Figure 3C. The XRD diffraction patterns of Ni and NiO appear to be in simple cubic and rhombohedral structures, with elemental Ni present in a significant amount. The reflection peaks for Ni is indexed entirely to face-centered-cubic (fcc) structure {space group: Fm3m (225)} of Ni nanocrystals having unit cell dimension: a = 3.5234 Å. Three peaks at 2θ = 44.5, 51.9, and 76.5 correspond to the diffraction from the {111, 200, 220} facets, respectively, and the peaks at 2θ = 37.28, 43.28, 62.88, 75.28 and 79.48 correspond to the diffraction from the {111, 200, 220, 311, 222} facets, respectively.

3.3 Self-assembled nanonetwork material properties and SERS Enhancement:

As shown in the inset of Figure 3, the Raman spectrum of crystalline Ni–NiO shows several bands in the probed region above 400 cm^{-1}. There are four peaks, 65 cm^{-1}, 1333 cm^{-1}, 1775 cm^{-1} and 2300 cm^{-1}. The peaks around 65 cm^{-1}, 1333 cm^{-1}, and 2300 cm^{-1} can be assigned to the 1st magnon (1MO), 2nd (2MO), and 4th (4MO) mode vibrations based on the literature [36–38]. The 3rd-magnon mode identified at 1776 cm^{-1} in the inset of figure 3A is consistently observed for a cuboidal nanonetwork and has never been reported in the existing literature.

Similarly, the peak found at 490 cm^{-1} is assigned to the one-phonon longitudinal optical (LO) and transverse optical (TO) mode of NiO, based on previous research by Ghandhi et al.[36], and the peak at 870 cm^{-1} is assigned to the two-phonon (2LO) mode based on the literature [38]. The first order Raman scattering peak at 490 cm^{-1} is slightly diminished and shifted when compared with the second order peak found at 870 cm^{-1}, implying a high nickel to nickel oxide vacancy concentration.

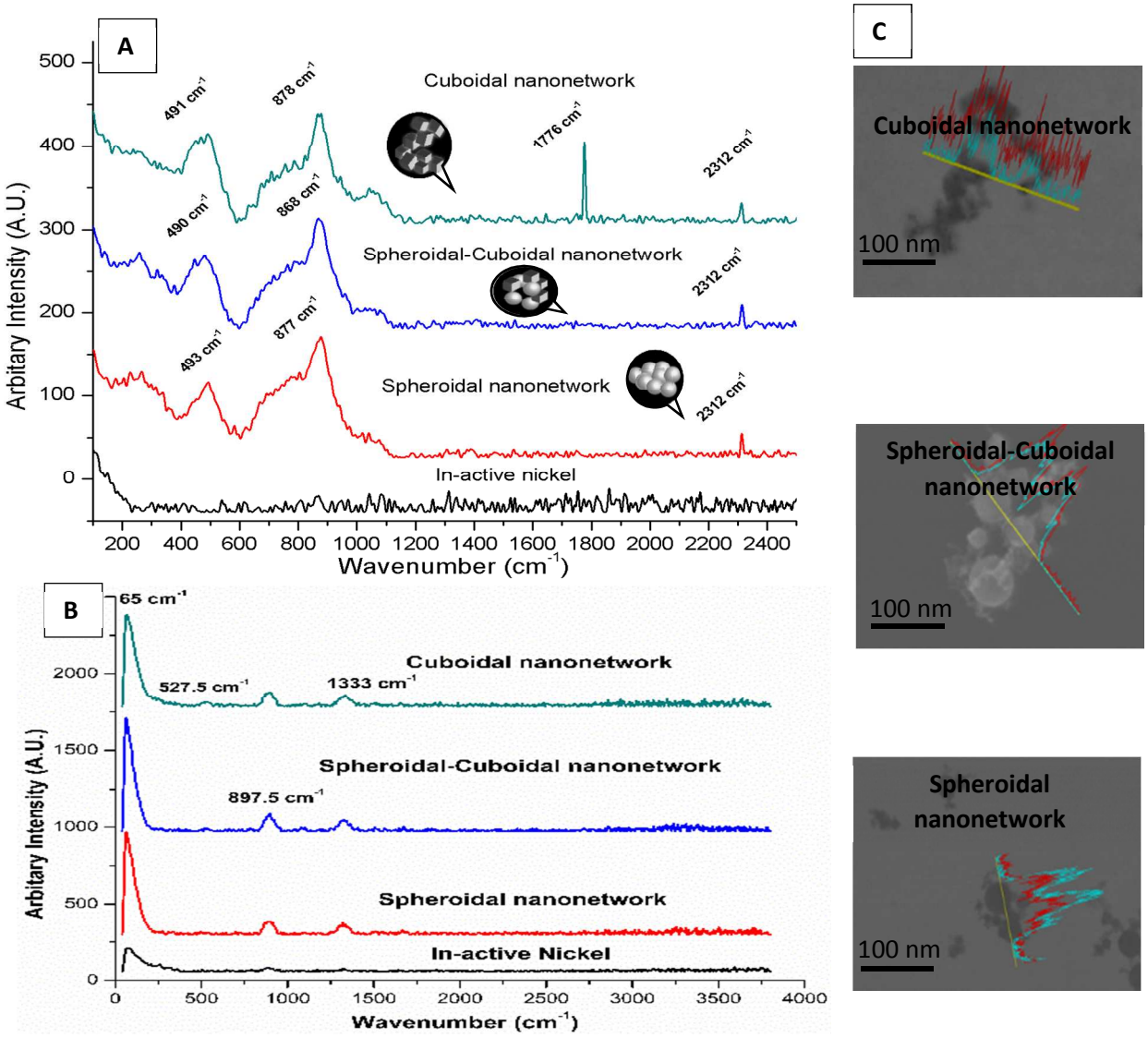

Figure 3: SERS activated nickel nanonetwork at cuboidal, spheroidal-cuboidal and spheroidal nanonetwork morphology along with inactive nickel substrate at A) 532 nm Raman laser excitation B) 785 nm Raman laser excitation and C) compositional analysis of corresponding nickel nanonetworks

3.4 Raman scattering effect of CV on Nickel nanonetwork:

Crystal violet is a common cationic dye with a symmetric molecular structure. The native bulk nickel substrate has no response to the presence of the CV dye. However, the dye-coated nickel nanonetwork evidently showcased the characteristic peaks for the associated dye at concentrations ranging from 10^{-3} M to 10^{-12} M. The SERS response to CV dye, enhanced by the nickel nanonetwork at the 532 nm wavelength of the Raman laser, is shown in the inset of Figure 4. The spectrum obtained have relative shifts in the peak positions and intensity owing to strong surface reactions induced between the interacting CV dye molecule and nanoparticles present within the nanonetwork. This in turn translates to the selective enhancement of dye peaks, which are not observed with other nanomaterials. The

Raman spectra of CV detected through the nanonetwork are shown in the inset of Figure S2. In general, the vibrations of the central carbon (C+) phenyl bonds are assigned from 100–400 cm^{-1} and phenyl vibrations are above 400 cm^{-1}. Yamada et al. used single crystalline metal oxide (e.g., NiO and TiO_2) substrates and observed enhanced Raman response of pyridine. The observed results indicate the dependency of the characteristic Raman intensity peaks of pyridine on metal oxides employed for SERS enhancement. The Raman spectrum of a given sample varies depending on the type of metal oxide adopted[39]. The efficiency of the charge transfer process completely depends on the vibronic coupling of the conduction and valence bands induced by NiO nanoparticle chains. When the dimensions of the synthesized nickel nanonetwork become comparable to the size of the Bhor radius, quantization occurs. This in turn forces a weak Raman response at energy transition levels in conduction, valance bands, and vibronic coupling.

Both millimolar and micromolar concentrations of CV dye induced Raman response until 1700 cm^{-1}. A sudden shift is observed in the Raman spectra collected at nano and picomolar concentrations with active peaks beyond 3000 cm^{-1}. The peak observed at both 900 cm^{-1} and 3200 cm^{-1} show aromatic (C–H) group in the out-of-plane bend and stretch mode type molecular vibrations. This strong Raman response in both

modes have never been reported. Lombardi and Birke asserted that an enhancement factor above 10^4 cannot solely result from charge transfer. The enhancement factor achieved here is in the order of 10^9. The strong enhancement observed here could be a combined effect of the charge transfer and “hot spot” [18].

3.5 Realizing biomolecule detection on nickel biochip:

GSH is an abundant non-protein-based thiol source with an intracellular concentration of ~10 mM present in most mammalian cells[40]. Glutathione levels present in cells can be related to specific diseases, such as cancer, Alzheimer, and Parkinson’s, as well as diseases caused by aging[41,42]. A variety of screening methods have now been developed to detect GSH levels, for instance, electrochemical analysis, fluorescence spectrometry[43–45], colloidal-particle-based colorimetric assays[23], enzyme linked immunosorbent assay (ELISA), and UV/vis spectrometry. These methods however yielded limited sensitivity with only μM and nM limit of detection (LOD) performed on substrates with the constraint of conducting an external analysis and quantification[46–50]. On a substrate, GSH has a natural tendency to promote the aggregation of noble metal nanoparticles, which usually result in a stronger electromagnetic effect. Therefore, SERS emerged recently as a new method of GSH detection on substrates. Metal colloids such as gold and silver are generally considered to have better SERS

enhancement with high reproducibility and manipulability. However, owing to colloidal aggregation induced by the analytes, spectra were highly unstable and reproducibility was poor[51–53].

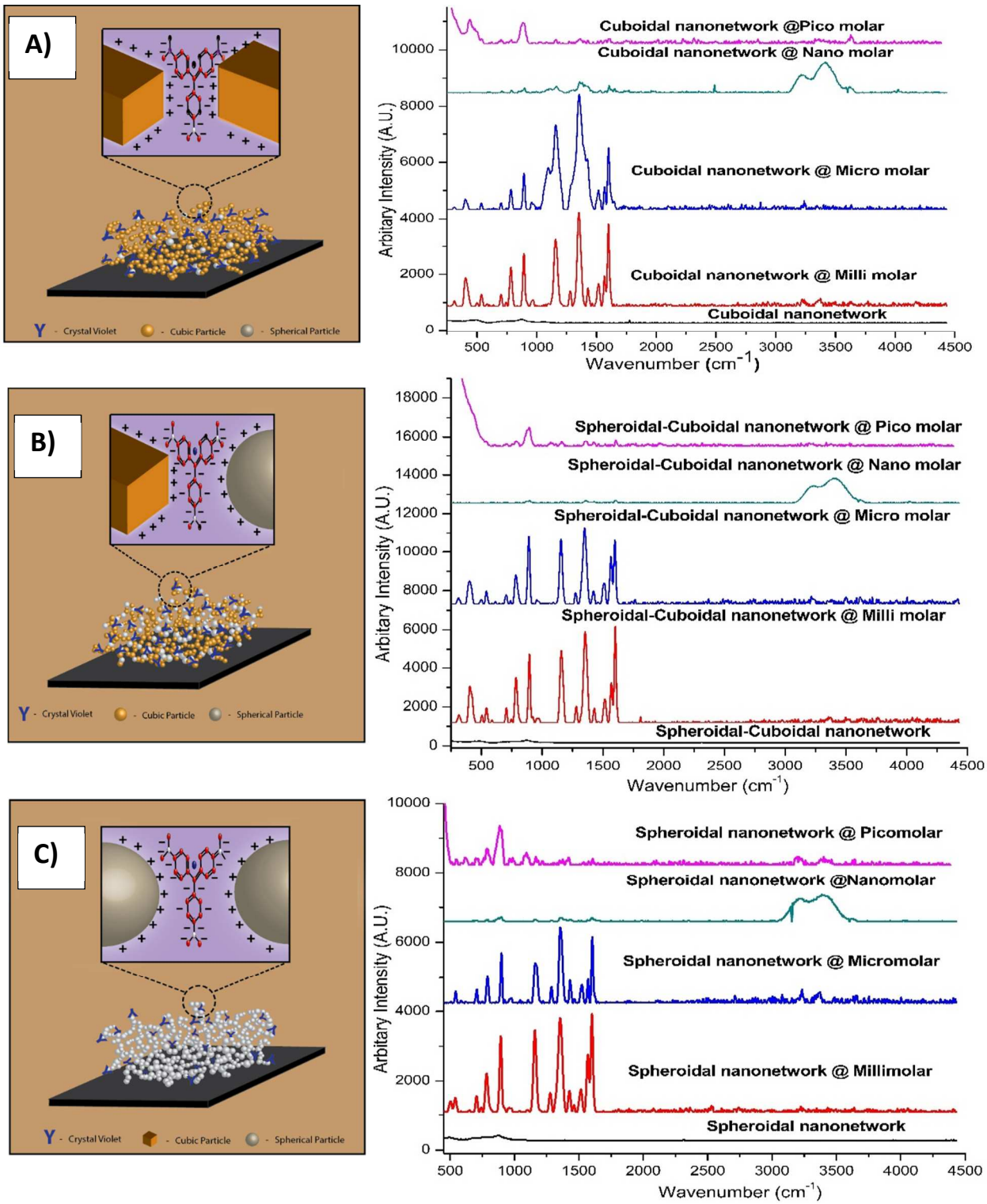

Figure 4: Functionalized Raman activation of synthesized nanonetwork with crystal violet from

millimolar to picomolar concentration for 532 nm Raman laser irradiation at A) Cuboidal nanonetwork B) Spheroidal-Cuboidal nanonetwork C) Spheroidal nanonetwork

The capability of the self-assembled 3D hybrid nickel nanonetwork for GSH biomolecule detection was tested. Figures 5 and S3 highlight the concentration profile of GSH where the response of GSH increases as the concentration decreases from the millimolar to picomolar range. The strongest spectra intensity was observed at picomolar concentrations for 532 and 785 nm Raman laser excitations. The detection limit of GSH biomolecule was at least 1 pM. A few of the most prominent bands for GSH biomolecule were observed between 890 and 3300 cm^{-1} for the 532 nm Raman laser wavelength in the inset of Figure S3. In

general, it is expected that most of the collected Raman spectra and SERS of polypeptides can be assigned based on their corresponding spectral amino acids[54].

Thus, those bands for GSH biomolecule may be associated with vibration modes of the sulfur atom present in the amino acids cysteine (Cys). The intensity of these Raman bands at different concentrations of GSH and the large enhancement for C–S stretching modes indicate that the sulfur atom present in GSH interacts strongly with the nickel nanonetworks. The strong spectral peaks of GSH appear around 3400 cm^{-1} for the 532 nm Raman laser excitation, representing O–H vibrations of carboxylic acids. The obtained signal-to-noise (SNR) ratio is 8.75, which is lower than that (SNR = 3) reported by Larsson et al. and Deregowska et al., who used a colloidal gold substrate as a primary source to enhance Raman peaks[47,55].

The Raman laser irradiation at 785 nm significantly enhanced the carboxyl group vibrations at 910 and 1320 cm^{-1}. The carboxylate groups can be assigned to the C–COO^- stretching vibrations and symmetry, respectively. Meanwhile, the bands originating from the N-terminal group are only present at picomolar concentrations for the 532 nm Raman laser irradiation in the spheroidal–cuboidal nanonetwork. This weak band at 1055 cm^{-1} is first assigned to the amino group, suggesting that GSH interacts with the nickel nanonetwork and not only through the carboxylate group, as suggested earlier by Meng Lv et al.[56], but other functional groups may also interact with Ni/NiO. The band appearing at 1633 cm^{-1} can be assigned to the first amide vibration. Their relative Raman intensity peaks are consistently weakly observed in all concentrations of GSH from the inset of Figure S3 and in Table S2.

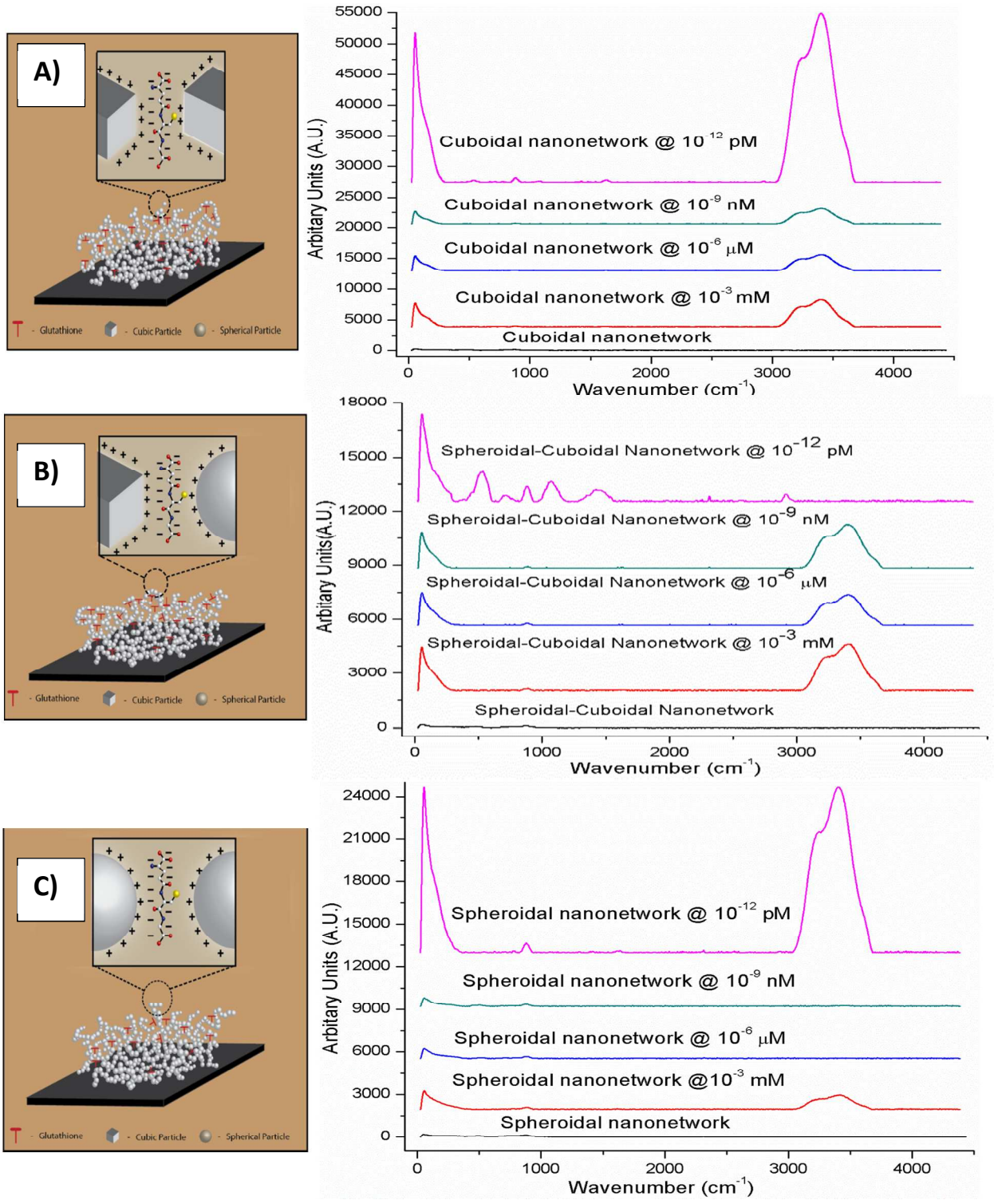

Figure 5: Functionalized Raman activation of synthesized nanonetwork with glutathione (GSH) biomolecule from millimolar to picomolar concentration for 532 nm Raman laser irradiation at A) Cuboidal nanonetwork B) Spheroidal-Cuboidal nanonetwork C) Spheroidal nanonetwork at 532 nm Raman laser irradiation

The sharp corners and edges of the cuboidal nanoparticles in the 3D network provided many sites that readily trap the analyte molecules. These aggregated molecules form “hot spots,” and this subsequently translates to large SERS enhancement factor per surface molecule. It is well-established that these “hot spots’’ contribute to SERS, and the enhancement due to the self-assembled nanostructures is about five orders of magnitude higher than that induced by isolated nanoparticles[57,58]. Although self-assembled nanostructures have been widely studied, the fabrication of controllable and reproducible “hot spots” remains a major challenge. Recently, He et al. demonstrated high SERS enhancement by fabricating arranged silver nanoparticles and gold nanorods embedded in polyvinyl alcohol (PVA) nanofibers through electrospinning[59].

The SERS spectrum at picomolar concentrations of GSH is strong and presented a variety of peaks up to 4000 cm^{-1}. In contrast, other methods normally generated only few weak Raman excitation peaks if active at picomolar concentrations. The high sensitivity of the 3D hybrid nickel nanonetwork can be attributed to the multiple E-field enhancements from nanoparticle crevice gaps, and to the mutual charge transfer between the dye molecule and the nanoparticle. For example, single crystalline Ag nanocubes generated using the polyol method yielded a 10^5 fold enhancement of rhodamine 6G analyte owing to a large number of generated Ag nanocubes acting as hotspot[58]. When compared to the traditional approach of using noble metal with gap plasmonics for SERS enhancement, the hybrid nickel nanonetwork provided multiple ‘’hot spots’’, leading to increased peaks of the spectrum.

3.6 Establishing nano-biosensor sensitivity and limit of detection:

Most established approaches (physical and chemical) employ prolonged incubation of target molecules and heating of the synthesized SERS platform to enhance the sensitivity and selectivity[60,61]. This entire process is eliminated with the 3D hybrid nickel nanonetwork, thereby providing instantaneous detection. The 3D nickel nanonetwork was used to test glutathione concentration varying from 1 mM to 1 pM. The characteristic intensity peak of GSH is observed at 3300 cm^{-1}, and at 1600cm^{-1} for CV for the 532 nm Raman laser excitation, as shown in the inset of Figure 6 and in Table S2. The cuboidal nanonetwork demonstrated the strongest enhancement at all GSH biomolecule concentrations from 1 mM to 1 pM. The spheroidal nanonetwork presented the least enhancement at higher (1 mM) dye concentrations but did not show any enhancement at both µM and nM GSH concentration suggesting that the enhancement observed at mM is due to analyte saturation only. However, a moderate enhancement was noticed at 1 pM GSH concentration indicating that the enhancement is due to charge transfer mechanism.

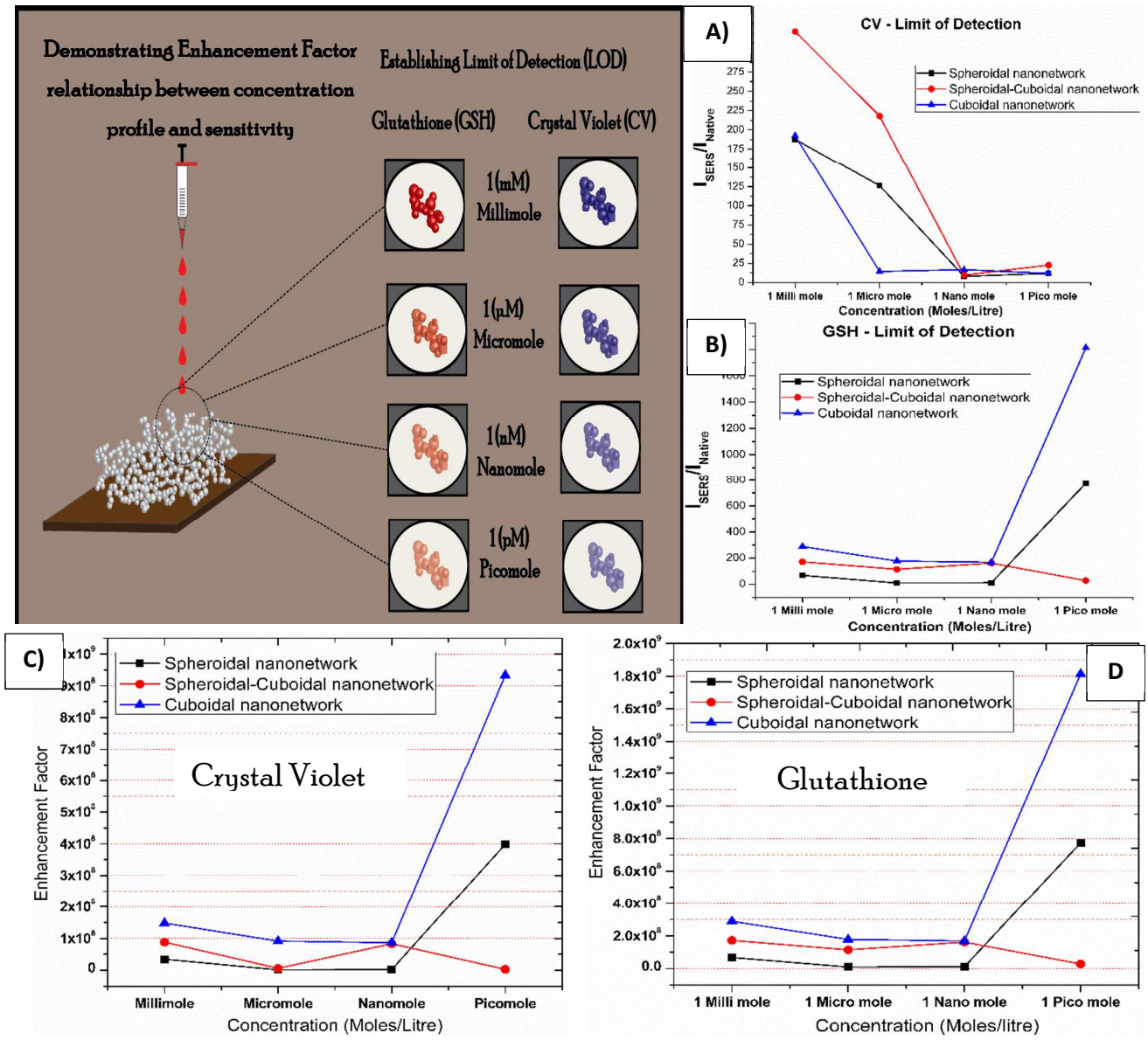

Figure 6: Limit of detection (LOD) established for Raman intensity plots of activated 3D hybrid nickel nanonetwork with different concentration profiles of A) Crystal Violet (CV) and B) Glutathione (GSH). Enhancement Factor (EF) of C) CV molecules at 1600 cm^{-1} and D) GSH molecules at 3300 cm^{-1} for different concentration profiles.

However, the spheroidal–cuboidal hybrid nanonetwork, which showed moderate enhancement at higher (1 mM) GSH biomolecule concentrations, presented the least enhancement at 1 pM, compared with the cuboidal and spheroidal nanonetwork. This reduced enhancement at high (1 mM) concentrations is influenced by a variety of factors, such as the nanomorphology and material oxide phase composition of the nickel nanonetworks. Jiwon Lee et al. reported 10 pM sensitive GSH biomolecule detection by varying the noble metal composition present in the nanostructure, thus implying the significance of material

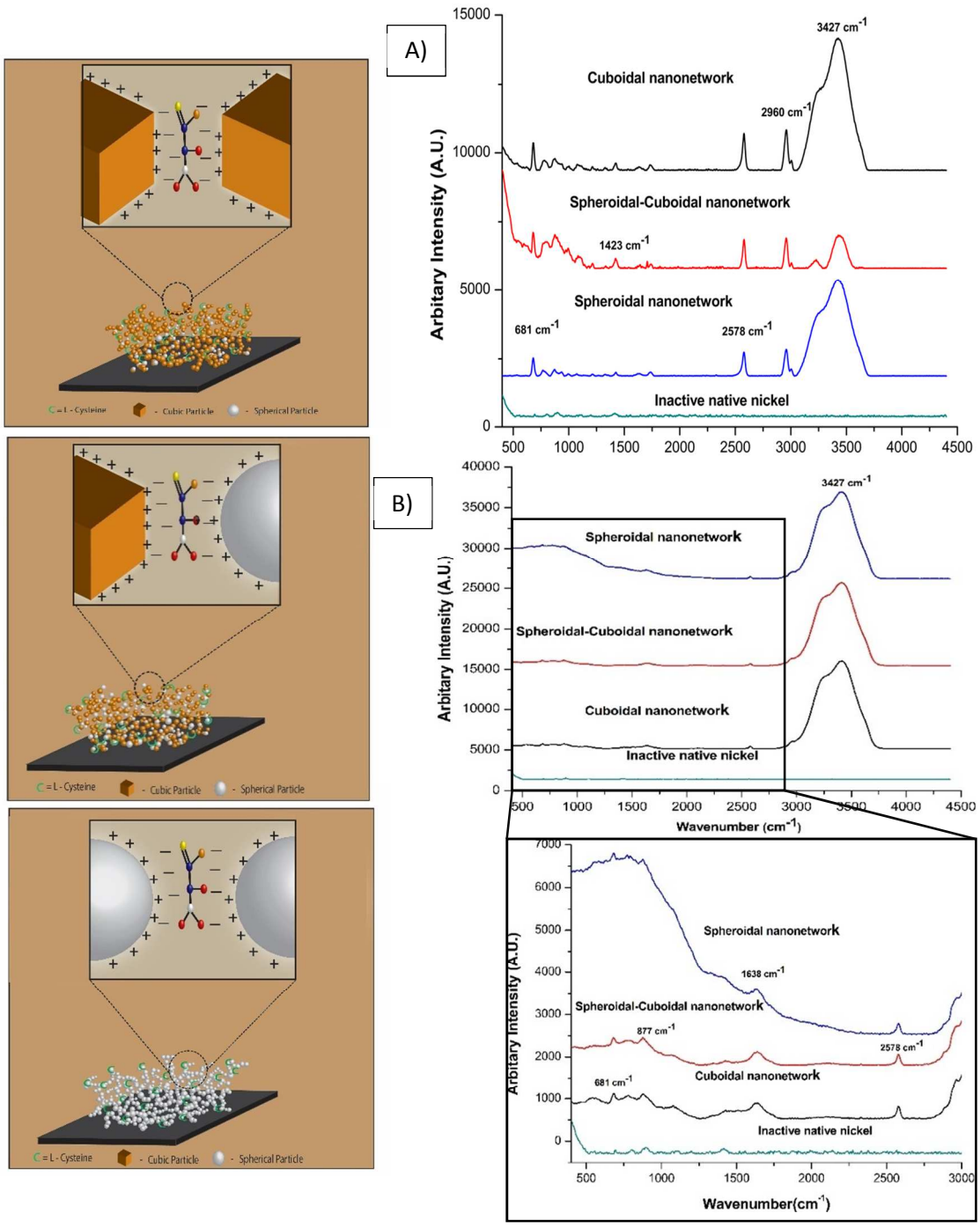

Figure 7: Functionalized Raman activation of synthesized nanonetwork with L-Cysteine (L-Cys) biomolecule for 532 nm Raman laser irradiation for Cuboidal nanonetwork, Spheroidal-Cuboidal nanonetwork and Spheroidal nanonetwork A) 1mM and B) 1µM concentration at 532 nm Raman laser irradiation.

composition in biomolecule sensing and enhancement[62]. Similarly, Guan et al. reported only a micromolar sensitive GSH biosensor using cuboidal gold nanoparticles[63].

Nevertheless, the nickel nanonetworks synthesized here could sense GSH biomolecules up to concentrations of 1 pM with an enhancement factor on the order of 10^9. To the best of our knowledge, this is the highest enhancement factor reported thus far with Raman spectra detection for GSH at concentration as low as 1 pM using non-noble-metal nanomaterials.

3.7 Accomplishing L-Cysteine and L-Methionine detection on nickel nano chips:

In order to show versatility of the nickel nanobiosensor synthesized, aqueous solutions of L-Cysteine (L-Cys) and L-Methionine (L-Met) biomolecules were tested individually on nickel nanobiosensor synthesized at 532 nm Raman laser excitations. Cysteine is responsible for stabilization of secondary protein structures and functions as a powerful antioxidant protecting the body against radiation, while Methionine aids in initiating the process of translation as messenger RNA[64]. The inactive native nickel substrate did not induce any Raman activity. However, the synthesized nickel nanonetwork induced strong SERS spectra response on each amino acid/biomolecules observed at both 1 millimolar and 1 micromolar concentrations which are presented in the inset of Figure 7 and 8. The collected spectra for L-Cys and L-Met are unique with enhancement/activation of bands exclusive to the biomolecule tested.

Most prominent bands for L-Cys biomolecule was observed at 681, 877, 1423, 1638, 2578, 2960 and 3427 cm^{-1} for 532nm Raman laser wavelength at both 1mM and 1µM concentration highlighted in the inset Figure 7. The series of bands observed at 681 cm^{-1}, 877 cm^{-1} and 1423 cm^{-1} are assigned to C-S, C-C stretching vibration and CH_2 bending vibration pertaining to L-Cys based on the work by Podstawka et al[64]. In addition, a series of sharp and strong bands were also observed at 1638, 2578 and 2960 cm^{-1}. The band at 1638 cm^{-1} can be assigned to carbonyl C=O asymmetric stretching vibration, while S-H stretching vibration can be assigned at 2578 cm^{-1} and lastly C-H stretching vibration assigned at 2960 cm^{-1} as earlier reported by Pawlukojć et al[65]. The nanonetwork distinctively induced sharp S-H stretching at 2578 cm^{-1} within 6 cm^{-1} signifying the complete absence of hydrogen bonding as reported by Edsall et al[66]. Additionally, broad band was observed at 3427 cm^{-1} which can be assigned to NH_3 asymmetric stretching vibration of L-Cys.

Likewise, SERS spectra of L-Met activated on nickel nanonetworks presented discernable peaks at 641, 704, 880, 1426 and 2929 cm^{-1} is presented in the inset Figure 8. Based on the work by Podstawka et al[64]., the band at 641 and 704 cm^{-1} are assigned to both carboxyl COO^- and C-S symmetric stretching vibrations. The bands at 880, 1426 and 2929 cm^{-1} is assigned to CH_2 rocking, CH_2 bending and CH_2 asymmetric stretching vibrations respectively from Zhu et al and Pandiarajan et al[67,68]. The strong peak at 2929 cm^{-1} assigned as CH_2 asymmetric stretching vibrations had difference in peak height exhibited

with L-Met for millimolar and micromolar concentrations. Also, the broad bands at 3233 and 3421 cm^{-1} can be assigned to stretching modes of N-H and NH_3 vibrations of L-Met[69].

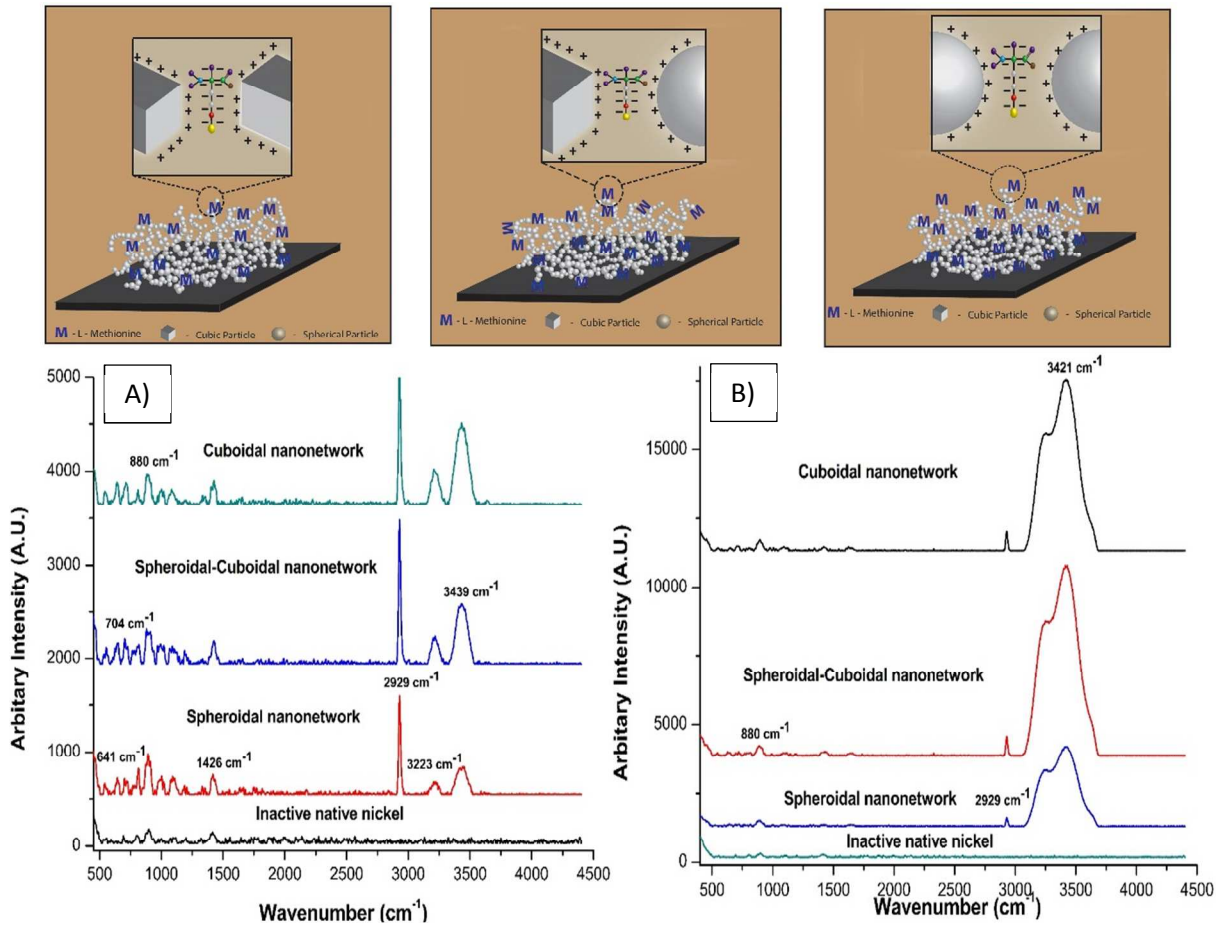

Figure 8: Functionalized Raman activation of synthesized nanonetwork with L-Methionine (L-Met) biomolecule for 532 nm Raman laser irradiation for Cuboidal nanonetwork, Spheroidal-Cuboidal nanonetwork and Spheroidal nanonetwork A) 1mM and B) 1µM concentration at 532 nm Raman laser irradiation.

3.8 Accomplishing GSH sensing in complex biological environment detection on nickel nano chips:

Cell culture medium contain all the elements that cells need for growth, sustained maintenance in laboratory environment mimicking real body conditions. The aim of this study is to find the selectivity of synthesized nickel nanonetwork in sensing GSH in complex biological environment. The SERS response to complex biological environment on nickel nanonetwork and inactive nickel substrate is presented in the inset of Figure 9A. Both the nanonetwork and inactive nickel substrate produced equal Raman response to the complex biological environment. Nevertheless, when 1 µM concentration of GSH biomolecule when added to this complex biological environment, it induced an idiosyncratic Raman response to the already synthesized nickel nanonetwork. A strong spectral peaks were noticed at 3416 cm^{-1} for all nickel nanonetworks at 532 nm Raman laser excitation along with other peaks contributed by

the complex biological environment also. This peak represents O–H vibrations of carboxylic acids present in GSH diluted in a complex biological environment. Thus, this study showcases the selectivity of synthesized nickel nanonetworks while sensing GSH in complex biological environment.

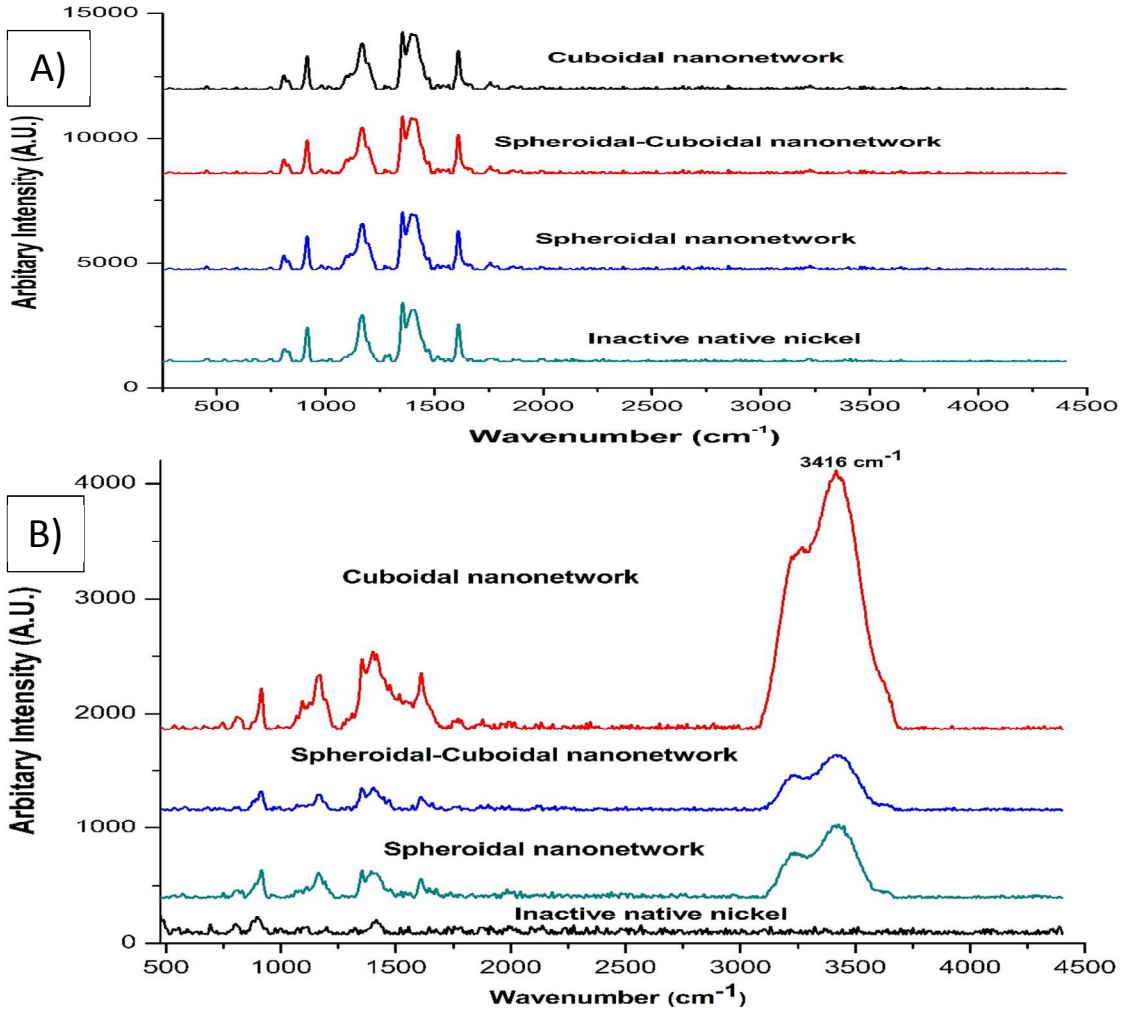

Figure 9: Functionalized Raman activation of synthesized nanonetwork Cuboidal nanonetwork, Spheroidal-Cuboidal nanonetwork and Spheroidal nanonetwork at A) complex biological environment (Cell culture medium) and B) 1µm concentration of GSH added to complex biological environment (Cell culture medium) at 532 nm Raman laser irradiation

4. Conclusions:

In summary, we have introduced a tunable "non-noble metal" based SERS active nano-biosensor chip for biomolecule detection using self-assembled 3D hybrid nickel nanonetworks. The nickel biochip synthesized with tunable physiochemical characteristics was functionalized by multiphoton ionization nanomaterials synthesis. With this nanobiosensor, Raman spectra were obtained for detection of CV dye molecules and GSH molecules at two Raman excitation wavelengths, namely 532 nm and 785 nm. The results showed a limit of detection of one picomolar (1 pM) for both GSH and CV with an enhancement

factor of 1.8 x 10^9 and 9.3 x 10^8. The versatility of this nanobiosensor was examined with biomolecules such as L-Cys and L-Met at 1mM and 1µM concentrations. In addition, the selectivity of the biosensor is now reported using 1µM concentration of GSH in a cell culture medium which mimics complex biological environment. This is the first time a "non-noble metal" based ultra-sensitive nano-biosensor platform was demonstrated. With high sensitivity and strong signal output at 532 nm and 785 nm excitations, this approach is promising for both in-vitro and in-vivo sensing applications.

5. Associated Content:

Supplementary information

Electronic supporting information (ESI) includes the following: Raman enhancement factor calculation, Table S1 - Compares laser parameters with synthesized nanonetwork nomenclature, Figure S1 - represent AFM height and phase analysis on synthesized nanonetwork, XRD spectrum of synthesized nanonetwork with corresponding Reitveld refinement, Figure S2 - show activated nickel nanonetwork interaction with crystal violet CV at 532 nm and 785 nm Raman excitation, Figure S3 - represent activated nickel nanonetwork interaction with Glutathione biomolecule at 532 nm and 785 nm Raman excitation, Table S2 - Raman excitation comparison based on nanonetwork composition vs GSH dye concentration. Table S3 - Comparison of the proposed method with other methods for biomolecule detection, Table S4 - Comparison of the proposed SERS based nano-biosensor with other SERS biosensors. Table S5 – Laser parameters with corresponding synthesized nanonetwork image and Energy Dispersive X-ray image of observed nanonetwork

6. Authors contributions:

Krishnan Venkatakrishnan is the corresponding author. Email: venkat@ryerson.ca Sivaprasad carried out laser fabrication of samples, material characterization and drafted the manuscript. Krishnan and Bo supported in its design and co-ordination. All authors read and approved the manuscript and declare that they have no competing interests.

7. Funding Source:

This research was funded by Natural Science and Engineering Research Council of Canada (NSERC Discovery Grant 126042, 119087).

8. Acknowledgements

The authors thank Mr. Advait Pai for his assistance with illustrations.

9. References:

(1) Manikandan, M.; Nasser Abdelhamid, H.; Talib, A.; Wu, H. F. Facile Synthesis of Gold Nanohexagons on Graphene Templates in Raman Spectroscopy for Biosensing Cancer and Cancer

Stem Cells. *Biosens. Bioelectron.* **2014**, *55*, 180–186.

(2) Saxena, U.; Das, A. B. Nanomaterials towards Fabrication of Cholesterol Biosensors: Key Roles and Design Approaches. *Biosens. Bioelectron.* **2016**, *75*, 196–205.

(3) Kang, Z.; Gu, Y.; Yan, X.; Bai, Z.; Liu, Y.; Liu, S.; Zhang, X.; Zhang, Z.; Zhang, X.; Zhang, Y. Enhanced Photoelectrochemical Property of ZnO Nanorods Array Synthesized on Reduced Graphene Oxide for Self-Powered Biosensing Application. *Biosens. Bioelectron.* **2014**, *64*, 499–504.

(4) Alubaidy, M.; Soleymani, L.; Venkatakrishnan, K.; Tan, B. Femtosecond Laser Nanostructuring for Femtosensitive DNA Detection. *Biosens. Bioelectron.* **2012**, *33* (1), 82–87.

(5) Stobiecka, M.; Hepel, M. Effect of Buried Potential Barrier in Label-Less Electrochemical Immunodetection of Glutathione and Glutathione-Capped Gold Nanoparticles. *Biosens. Bioelectron.* **2011**, *26* (8), 3524–3530.

(6) Ding, Y.; Liu, J.; Wang, H.; Shen, G.; Yu, R. A Piezoelectric Immunosensor for the Detection of α-Fetoprotein Using an Interface of Gold/hydroxyapatite Hybrid Nanomaterial. *Biomaterials* **2007**, *28* (12), 2147–2154.

(7) Buryakov, I. A.; Buryakov, T. I.; Matsayev, V. T. Electrical, Electrochemical, and Thermometric Sensors for the Detection of Explosives. *J. Anal. Chem.* **2016**, *71* (3), 234–242.

(8) Kang, H.; Jeong, S.; Park, Y.; Yim, J.; Jun, B.-H.; Kyeong, S.; Yang, J.-K.; Kim, G.; Hong, S.; Lee, L. P.; Kim, J.-H.; Lee, H.-Y.; Jeong, D. H.; Lee, Y.-S. Near-Infrared SERS Nanoprobes with Plasmonic Au/Ag Hollow-Shell Assemblies for In Vivo Multiplex Detection. *Adv. Funct. Mater.* **2013**, *23* (30), 3719–3727.

(9) Stobiecka, M.; Hepel, M. Rapid Functionalization of Metal Nanoparticles by Moderator-Tunable Ligand-Exchange Process for Biosensor Designs. *Sensors Actuators, B Chem.* **2010**, *149* (2), 373–380.

(10) Stobiecka, M. Novel Plasmonic Field-Enhanced Nanoassay for Trace Detection of Proteins. *Biosens. Bioelectron.* **2014**, *55*, 379–385.

(11) Culha, M.; Cullum, B.; Lavrik, N.; Klutse, C. K. Surface-Enhanced Raman Scattering as an Emerging Characterization and Detection Technique. *J. Nanotechnol.* **2012**, *2012*, 1–15.

(12) Maznichenko, D.; Venkatakrishnan, K.; Tan, B. Stimulating Multiple SERS Mechanisms by a Nanofibrous Three-Dimensional Network Structure of Titanium Dioxide (TiO 2). *J. Phys. Chem. C* **2013**, *117* (1), 578–583.

(13) Li, W.; Zamani, R.; Rivera Gil, P.; Pelaz, B.; Ibáñez, M.; Cadavid, D.; Shavel, A.; Alvarez-Puebla, R. A.; Parak, W. J.; Arbiol, J.; Cabot, A. CuTe Nanocrystals: Shape and Size Control, Plasmonic

Properties, and Use as SERS Probes and Photothermal Agents. *J. Am. Chem. Soc.* **2013**, *135* (19), 7098–7101.

(14) Register, J. K.; Fales, A. M.; Wang, H.-N.; Norton, S. J.; Cho, E. H.; Boico, A.; Pradhan, S.; Kim, J.; Schroeder, T.; Wisniewski, N. A.; Klitzman, B.; Vo-Dinh, T. In Vivo Detection of SERS-Encoded Plasmonic Nanostars in Human Skin Grafts and Live Animal Models. *Anal. Bioanal. Chem.* **2015**, *407* (27), 8215–8224.

(15) Xu, W.; Ling, X.; Xiao, J.; Dresselhaus, M. S.; Kong, J.; Xu, H.; Liu, Z.; Zhang, J. Surface Enhanced Raman Spectroscopy on a Flat Graphene Surface. *Proc. Natl. Acad. Sci.* **2012**, *109* (24), 9281–9286.

(16) Zhang, Y.; Wang, C.; Wang, J.; Chen, L.; Li, J.; Liu, Y.; Zhao, X.; Wang, Y.; Yang, J. Nanocap Array of Au:Ag Composite for Surface-Enhanced Raman Scattering. *Spectrochim. Acta - Part A Mol. Biomol. Spectrosc.* **2016**, *152*, 461–467.

(17) Mao, Z.; Song, W.; Chen, L.; Ji, W.; Xue, X.; Ruan, W.; Li, Z.; Mao, H.; Ma, S.; Lombardi, J. R.; Zhao, B. Metal–Semiconductor Contacts Induce the Charge-Transfer Mechanism of Surface-Enhanced Raman Scattering. *J. Phys. Chem. C* **2011**, *115* (37), 18378–18383.

(18) Lombardi, J. R.; Birke, R. L. The Theory of Surface-Enhanced Raman Scattering. *J. Chem. Phys.* **2012**, *136* (14), 144704.

(19) Wang, D.; Zhu, W.; Best, M. D.; Camden, J. P.; Crozier, K. B. Directional Raman Scattering from Single Molecules in the Feed Gaps of Optical Antennas. *Nano Lett.* **2013**, *13* (5), 2194–2198.

(20) Cortés, E.; Etchegoin, P. G.; Le Ru, E. C.; Fainstein, A.; Vela, M. E.; Salvarezza, R. C. Monitoring the Electrochemistry of Single Molecules by Surface-Enhanced Raman Spectroscopy. *J. Am. Chem. Soc.* **2010**, *132* (51).

(21) Sarkar, S.; Dutta, S.; Pal, T. Tailored “Sandwich” Strategy in Surface Enhanced Raman Scattering: Case Study with Para -Phenylenediamine and Application in Femtomolar Detection of Melamine. *J. Phys. Chem. C* **2014**, *118* (48), 28152–28161.

(22) Wen, C.; Liao, F.; Liu, S.; Zhao, Y.; Kang, Z.; Zhang, X.; Shao, M. Bi-Functional ZnO–RGO–Au Substrate: Photocatalysts for Degrading Pollutants and SERS Substrates for Real-Time Monitoring. *Chem. Commun.* **2013**, *49* (29), 3049.

(23) Zhong, Z.; Luo, J.; Ang, T. P.; Highfield, J.; Lin, J.; Gedanken, A. Controlled Organization of Au Colloids into Linear Assemblies. *J. Phys. Chem. B* **2004**, *108* (47), 18119–18123.

(24) Li, Y.; Liu, Q.; Shen, W. Morphology-Dependent Nanocatalysis: Metal Particles. *Dalt. Trans.* **2011**, *40* (22), 5811.

(25) Shen, H.; Lu, G.; Zhang, T.; Liu, J.; Gu, Y.; Perriat, P.; Martini, M.; Tillement, O.; Gong, Q. Shape Effect on a Single-Nanoparticle-Based Plasmonic Nanosensor. *Nanotechnology* **2013**, *24* (28), 285502.

(26) Wang, X.; Shi, W.; She, G.; Mu, L. Surface-Enhanced Raman Scattering (SERS) on Transition Metal and Semiconductor Nanostructures. *Phys. Chem. Chem. Phys.* **2012**, *14* (17), 5891.

(27) Wu, J.; Zhou, W.; Cheng, Q.; Yang, J. Polyvinylpyrrolidone-Stabilized Magnetic Nickel Nanochains for Cancer Hyperthermia and Catalysis Applications. *RSC Adv.* **2015**, *5* (29), 22965–22971.

(28) Kumar, G. V. P. Plasmonic Nano-Architectures for Surface Enhanced Raman Scattering: A Review. *J. Nanophotonics* **2012**, *6* (1), 64503.

(29) Bayata, F.; Akinci, Z. B.; Donatan, A. S.; Urgen, M. A Novel Free-Standing Nanowire Substrate with Surface Enhanced Raman Scattering (SERS) Activity. *Mater. Lett.* **2012**, *67* (1), 387–389.

(30) Sajanlal, P. R.; Pradeep, T. Functional Hybrid Nickel Nanostructures as Recyclable SERS Substrates: Detection of Explosives and Biowarfare Agents. *Nanoscale* **2012**, *4* (11), 3427.

(31) Manoj, K.; Gayathri, S.; Jayabal, P.; Ramakrishnan, V. Synthesis and Characterization of Ni/Ag Nanocomposite for Surface Enhanced Raman Scattering Measurement. *Mater. Res. Express* **2015**, *2* (6), 65003.

(32) Sivakumar, M.; Venkatakrishnan, K.; Tan, B. Study of Metallic Fibrous Nanoparticle Aggregate Produced Using Femtosecond Laser Radiation under Ambient Conditions. *Nanotechnology* **2010**, *21* (22), 225601.

(33) Sivakumar, M.; Venkatakrishnan, K.; Tan, B. Characterization of MHz Pulse Repetition Rate Femtosecond Laser-Irradiated Gold-Coated Silicon Surfaces. *Nanoscale Res. Lett.* **2011**, *6* (1), 78.

(34) Shoute, L. C. T.; Bergren, A. J.; Mahmoud, A. M.; Harris, K. D.; McCreery, R. L. Optical Interference Effects in the Design of Substrates for Surface-Enhanced Raman Spectroscopy. *Appl. Spectrosc.* **2009**, *63* (2), 133–140.

(35) Jensen, T.; Jensen, T.; Kelly, K. L.; Kelly, K. L.; Lazarides, a.; Lazarides, a.; Schatz, G. C.; Schatz, G. C. Electrodynamics of Noble Metal Nanoparticles and Nanoparticle Clusters. *J. Clust. Sci.* **1999**, *10* (2), 295–317.

(36) Gandhi, A.; Huang, C.-Y.; Yang, C.; Chan, T.; Cheng, C.-L.; Ma, Y.-R.; Wu, S. Growth Mechanism and Magnon Excitation in NiO Nanowalls. *Nanoscale Res. Lett.* **2011**, *6* (1), 485.

(37) Marciuš, M.; Ristić, M.; Ivanda, M.; Musić, S. Formation and Microstructure of Nickel Oxide Films. *J. Alloys Compd.* **2012**, *541*, 238–243.

(38) Mironova-Ulmane, N.; Kuzmin, A.; Steins, I.; Grabis, J.; Sildos, I.; Pärs, M. Raman Scattering in

Nanosized Nickel Oxide NiO. *J. Phys. Conf. Ser.* **2007**, *93*, 12039.

(39) Yamada, H.; Yamamoto, Y. Surface Enhanced Raman Scattering (SERS) of Chemisorbed Species on Various Kinds of Metals and Semiconductors. *Surf. Sci.* **1983**, *134* (1), 71–90.

(40) Balendiran, G. K.; Dabur, R.; Fraser, D. The Role of Glutathione in Cancer. *Cell Biochem. Funct.* **2004**, *22* (6), 343–352.

(41) Meister, A.; Anderson, M. E. Glutathione. *Annu. Rev. Biochem.* **1983**, *52* (1), 711–760.

(42) Bains, J. S.; Shaw, C. A. Neurodegenerative Disorders in Humans: The Role of Glutathione in Oxidative Stress-Mediated Neuronal Death. *Brain Res. Rev.* **1997**, *25* (3), 335–358.

(43) Han, B.; Yuan, J.; Wang, E. Sensitive and Selective Sensor for Biothiols in the Cell Based on the Recovered Fluorescence of the CdTe Quantum Dots-Hg(II) System. *Anal. Chem.* **2009**, *81* (13), 5569–5573.

(44) Zhang, X.; Wu, F. G.; Liu, P.; Gu, N.; Chen, Z. Enhanced Fluorescence of Gold Nanoclusters Composed of HAuCl4 and Histidine by Glutathione: Glutathione Detection and Selective Cancer Cell Imaging. *Small* **2014**, *10* (24), 5170–5177.

(45) Tian, D.; Qian, Z.; Xia, Y.; Zhu, C. Gold Nanocluster-Based Fluorescent Probes for near-Infrared and Turn-on Sensing of Glutathione in Living Cells. *Langmuir* **2012**, *28* (8), 3945–3951.

(46) Huang, G. G.; Han, X. X.; Hossain, M. K.; Ozaki, Y. Development of a Heat-Induced Surface-Enhanced Raman Scattering Sensing Method for Rapid Detection of Glutathione in Aqueous Solutions. *Anal. Chem.* **2009**, *81* (14), 5881–5888.

(47) Larsson, M.; Lindgren, J. Analysis for Glutathione and Immunoglobulin G inside Chromatographic Beads Using Surface-Enhanced Raman Scattering Spectroscopy. *J. Raman Spectrosc.* **2005**, *36* (5), 394–399.

(48) Saha, A.; Jana, N. R. Detection of Cellular Glutathione and Oxidized Glutathione Using Magnetic-Plasmonic Nanocomposite-Based “turn-Off” surface Enhanced Raman Scattering. *Anal. Chem.* **2013**, *85* (19), 9221–9228.

(49) Cai, Q.-Y.; Li, J.; Ge, J.; Zhang, L.; Hu, Y.-L.; Li, Z.-H.; Qu, L.-B. A Rapid Fluorescence “switch-On” assay for Glutathione Detection by Using Carbon Dots-MnO2 Nanocomposites. *Biosens. Bioelectron.* **2015**, *72*, 31–36.

(50) Martinez-Garcia, M. M.; Cardoso-Avila, P. E.; Pichardo-Molina, J. L. Concave Gold Nanocubes on Al-6063 Alloy as a Simple and Efficient SERS Substrate. *Colloids Surfaces A Physicochem. Eng. Asp.* **2016**, *493* (493), 66–73.

(51) Dou, X.; Jung, Y. M.; Cao, Z.-Q.; Ozaki, Y. Surface-Enhanced Raman Scattering of Biological

Molecules on Metal Colloid II: Effects of Aggregation of Gold Colloid and Comparison of Effects of pH of Glycine Solutions between Gold and Silver Colloids. *Appl. Spectrosc.* **1999**, *53* (11), 1440–1447.

(52) Jing, C.; Fang, Y. Simple Method for Electrochemical Preparation of Silver Dendrites Used as Active and Stable SERS Substrate. *J. Colloid Interface Sci.* **2007**, *314* (1), 46–51.

(53) Guo, Z.; Liu, Z.-G.; Yao, X.-Z.; Zhang, K.-S.; Chen, X.; Liu, J.-H.; Huang, X.-J. A Molecular-Gap Device for Specific Determination of Mercury Ions. *Sci. Rep.* **2013**, *3*, 30–34.

(54) Brambilla, a.; Philippidis, A.; Nevin, A.; Comelli, D.; Valentini, G.; Anglos, D. Adapting and Testing a Portable Raman Spectrometer for SERS Analysis of Amino Acids and Small Peptides. *J. Mol. Struct.* **2013**, *1044*, 121–127.

(55) Der, A.; Depciuch, J.; Wojnarowska, R.; Polit, J.; Broda, D.; Nechai, H.; Gonchar, M.; Sheregii, E.; Samples, A. Study of Optical Properties of a Glutathione Capped Gold Nanoparticles Using Linker (MHDA) by Fourier Transform Infra Red Spectroscopy and Surface Enhanced Raman Scattering. *Int. J. Biol. Biomol. Agric. Food Biotechnol. Eng.* **2013**, *7* (1), 1–4.

(56) Lv, M.; Gu, H.; Yuan, X.; Gao, J.; Cai, T. Investigation of 3D Silvernanodendrite@glass as Surface-Enhanced Raman Scattering Substrate for the Detection of Sildenafil and GSH. *J. Mol. Struct.* **2012**, *1029*, 75–80.

(57) Qian, K.; Liu, H.; Yang, L.; Liu, J. Designing and Fabricating of Surface-Enhanced Raman Scattering Substrate with High Density Hot Spots by Polyaniline Template-Assisted Self-Assembly. *Nanoscale* **2012**, *4* (20), 6449.

(58) Lee, H. K.; Lee, Y. H.; Zhang, Q.; Phang, I. Y.; Tan, J. M. R.; Cui, Y.; Ling, X. Y. Superhydrophobic Surface-Enhanced Raman Scattering Platform Fabricated by Assembly of Ag Nanocubes for Trace Molecular Sensing. *ACS Appl. Mater. Interfaces* **2013**, *5* (21), 11409–11418.

(59) He, D.; Hu, B.; Yao, Q.; Wang, K.; Yu, S. Large-Scale Synthesis of Flexible Free- Sensitivity : Electrospun PVA Nanofibers of Silver Nanoparticles. *ACS Nano* **2009**, *3* (12), 3993–4002.

(60) Li, J.; Chen, L.; Lou, T.; Wang, Y. Highly Sensitive SERS Detection of As3+ Ions in Aqueous Media Using Glutathione Functionalized Silver Nanoparticles. *ACS Appl. Mater. Interfaces* **2011**, *3* (10), 3936–3941.

(61) Liu, R.; Si, M.; Kang, Y.; Zi, X.; Liu, Z.; Zhang, D. A Simple Method for Preparation of Ag Nanofilm Used as Active, Stable, and Biocompatible SERS Substrate by Using Electrostatic Self-Assembly. *J. Colloid Interface Sci.* **2010**, *343* (1), 52–57.

(62) Lee, J.; Zhang, Q.; Park, S.; Choe, A.; Fan, Z.; Ko, H. Particle–Film Plasmons on Periodic Silver Film

over Nanosphere (AgFON): A Hybrid Plasmonic Nanoarchitecture for Surface-Enhanced Raman Spectroscopy. *ACS Appl. Mater. Interfaces* **2016**, *8* (1), 634–642.

(63) Guan, Z.; Li, S.; Cheng, P. B. S.; Zhou, N.; Gao, N.; Xu, Q.-H. Band-Selective Coupling-Induced Enhancement of Two-Photon Photoluminescence in Gold Nanocubes and Its Application as Turn-on Fluorescent Probes for Cysteine and Glutathione. *ACS Appl. Mater. Interfaces* **2012**, *4* (10), 5711–5716.

(64) Podstawka, E.; Ozaki, Y.; Proniewicz, L. M. Part I: Surface-Enhanced Raman Spectroscopy Investigation of Amino Acids and Their Homodipeptides Adsorbed on Colloidal Silver. *Appl. Spectrosc.* **2004**, *58* (5), 570–580.

(65) Pawlukojć, A.; Leciejewicz, J.; Ramirez-Cuesta, A. J.; Nowicka-Scheibe, J. L-Cysteine: Neutron Spectroscopy, Raman, IR and Ab Initio Study. *Spectrochim. Acta Part A Mol. Biomol. Spectrosc.* **2005**, *61* (11–12), 2474–2481.

(66) Edsall, J. T.; Otvos, J. W.; Rich, A. Raman Spectra of Amino Acids and Related Compounds. VII. Glycylglycine, Cysteine, Cystine and Other Amino Acids. *J. Am. Chem. Soc.* **1950**, *72* (1), 474–477.

(67) Zhu, G.; Zhu, X.; Fan, Q.; Wan, X. Raman Spectra of Amino Acids and Their Aqueous Solutions. *Spectrochim. Acta - Part A Mol. Biomol. Spectrosc.* **2011**, *78* (3), 1187–1195.

(68) Pandiarajan, S.; Umadevi, M.; Briget Mary, M.; Rajaram, R. K.; Ramakrishnan, V. Infrared and Raman Spectroscopic Studies ofL-Methioninium Nitrate. *J. Raman Spectrosc.* **2004**, *35* (11), 907–913.

(69) Ghazaryan, V. V; Zakharov, B. A.; Boldyreva, E. V; Petrosyan, A. M. L-Methioninium Picrate. *Spectrochim. Acta - Part A Mol. Biomol. Spectrosc.* **2015**, *142*, 344–349.

Table of Contents Graphic